TIME TO APPROACH SIMILARITY

by JOSEPH J. WEBBER†

(*Trinity College, University of Cambridge, Trinity Street, Cambridge CB2 1TQ, UK; Institute of Theoretical Geophysics, Department of Applied Mathematics and Theoretical Physics, Centre for Mathematical Sciences, University of Cambridge, Wilberforce Road, Cambridge CB3 0WA, UK*)

and

HERBERT E. HUPPERT

(*King's College, University of Cambridge, King's Parade, Cambridge CB2 1ST, UK; Institute of Theoretical Geophysics, Department of Applied Mathematics and Theoretical Physics, Centre for Mathematical Sciences, University of Cambridge, Wilberforce Road, Cambridge CB3 0WA, UK*)

[Received 10 March 2019. Revise 9 September 2019. Accepted 10 September 2019]

Summary

In a recent article, Ball and Huppert (*J. Fluid Mech.*, **874**, 2019) introduced a novel method for ascertaining the characteristic timescale over which the similarity solution to a given time-dependent nonlinear differential equation converges to the actual solution, obtained by numerical integration, starting from given initial conditions. In this article, we apply this method to a range of different partial differential equations describing propagating gravity currents of fixed volume as well as modifying the techniques to apply to situations for which convergence to the numerical solution is oscillatory, as appropriate for gravity currents propagating at large Reynolds numbers. We investigate properties of convergence in all of these cases, including how different initial geometries affect the rate at which the two solutions agree. It is noted that geometries where the flow is no longer unidirectional take longer to converge. A method of time-shifting the similarity solution is introduced to improve the accuracy of the approximation given by the similarity solution, and also provide an upper bound on the percentage disagreement over all time.

1. Introduction

A large number of problems in the physical sciences require the solution of time-dependent nonlinear partial differential equations. A prime example in fluid mechanics is gravity currents, where fluids of different densities flow, primarily horizontally, into each other. This behaviour is important to understand in many different circumstances—Huppert (1) lists applications as varied as atmospheric flows, lava flows, the spreading of honey on toast and oceanic flows. However, all too often, numerical solutions to the governing nonlinear equations must be sought, because there are no analytical solutions.

In spite of this, in many cases a similarity solution can be found to the nonlinear equations, and the flow will tend towards the behaviour described by this solution for very large times. These solutions do not take into account the initial conditions, and there is no trivial manner of deciding when this similarity solution behaviour applies well to the flow (behaviour may agree with the

† <jw948@cam.ac.uk>

Q. Jl Mech. Appl. Math, Vol. 73. No. 1
Advance Access publication 11 October 2019. doi:10.1093/qjmam/hbz019

similarity solution to a high degree only after milliseconds or years, dependent on the situation and physical parameters). Therefore, a method of calculating how much time needs to pass until certain properties of real-life flows agree to within a given percentage with those of the similarity solution—an equilibration time—is sought.

A recent article by Ball and Huppert (2) presents a method for ascertaining the equilibration time for an axisymmetric viscous gravity current flowing above a rigid, horizontal boundary with given initial conditions. Considering a relatively long and thin viscous gravity current comprising two fluids with density difference $\Delta\rho$, with the more viscous fluid having dynamic viscosity μ, Huppert (3) derives,

$$\frac{\partial h}{\partial t} - \frac{\beta}{r}\frac{\partial}{\partial r}\left(rh^3\frac{\partial h}{\partial r}\right) = 0, \tag{1.1a}$$

to describe the height $h(r,\ t)$ of the intruding flow, subject to the volume remaining constant,

$$2\pi\int_0^{r_N(t)} rh(r,\ t)\ dr = V \tag{1.1b}$$

and

$$h(r_N) = 0, \tag{1.1c}$$

where $\beta = g\Delta\rho/(3\mu)$, and $r_N(t)$ is the maximum radial extent of the intruding flow. A similarity solution for r_N was first presented in (3). We now seek an equilibration time τ, which is a characteristic timescale for the actual value of r_N and the similarity solution r_s to agree to some fixed degree.

In (2), this agreement is measured by percentage difference relative to the similarity solution, p, a convention we will adopt here. Specifically,

$$p = \frac{100\,|r_s(t) - r_N(t)|}{r_s(t)}. \tag{1.2}$$

To derive their result, the hypothesis that τ is infinite for zero p (that is to say, the similarity solution never exactly reaches the numerical solution) and τ is a monotonically decreasing function of p (it takes more time to reach the result to a closer degree) are made, and then confirmed by numerical results for the problem (1.1).

The only parameters involved in the problem which could contribute to the equilibration time are β and V, where the dimensions of β are $(LT)^{-1}$, and those of V L^3, so it is reasonable to assume the equilibration time $\tau \propto 1/(\beta V^{1/3})$—as is shown to be the case by (2).

In this article, we will continue this approach and verify its use for finding equilibration times for other kinds of gravity currents, starting with those posed by (2). We note that equilibration times τ are approximately proportional to p^{-1} in all three of these canonical cases. The dependence of the equilibration time on the geometry of the initial problem, and how this changes based on the problem itself, will be discussed, with the strength of this dependence shown to differ greatly between different flows. We will then move on to consider similarity solutions of the shallow-water equations, much-discussed by others, including Hoult (4), Huppert and Simpson (5) and Grundy and Rottman

(6), and seek expressions for equilibration times in spite, in some cases, of the oscillatory nature of convergence to the similarity solution.

As well as investigating the characteristic times for convergence to the similarity solution in this oscillatory case, we will consider the nature of convergence in more depth here. We find that p can be zero for a series of finite times, as well as when $t \to \infty$. We investigate the minimum percentage differences at various stages of the oscillatory convergence, and how these relate to the parameters of the flow, and show that a modified form of the analysis detailed above can still be applied in this case, in spite of the large differences in the nature of convergence. It is also seen that the timescale for convergence depends on the specific initial dimensions of the flow, and not just on the initial aspect ratio, as was the case for monotonic convergence.

Furthermore, it is noted that the equilibration time no longer grows as p^{-1} in this non-monotonic case—by comparison with the analytic approach detailed by Grundy and Rottman (6), an approximate expression for the equilibration time as a function of p is derived for early times (which only holds for small times).

We also show that a simple modification of the similarity solutions for r_N, time-shifting them such that they match the initial value of r_N for the problem in question, generally provides a better approximation to the actual behaviour of the flow in cases where convergence is monotonic, therefore reducing the equilibration time. Furthermore, we investigate the maximum percentage difference over all time between this shifted similarity solution and the actual solution of the nonlinear equations, again for monotonic convergence.

2. Some canonical problems

In the Appendix of (2), three canonical problems are presented and general suppositions made as to the relationship between τ and the parameters of the problems. These problems are: two-dimensional (2D) viscous gravity currents; 2D gravity currents in a porous medium; and then axisymmetric currents in a porous medium. We solve all of these cases numerically, using a Crank–Nicolson predictor–corrector method with variable step sizes, to show that the suggested relationships do indeed hold.

We also find approximations to the relation between equilibration time τ and percentage difference p between the similarity solution and numerical solution. In all of the cases here, we show that τ is approximately proportional to $1/p$ for small p. Unless otherwise stated, we will be concentrating on $\tau_{5\%}$, that is to say, the time taken for the percentage difference p to be equal to five per cent. A difference of five per cent was chosen as a value close enough to zero to likely model behaviour for small p well, without having to perform the numerical integration for too long and risk introducing round-off errors.

2.1 *2D viscous gravity currents*

The governing equations in this case, denoting the maximum extent of the flow in the x-direction by $x_N(t)$ (and therefore introducing a similarity solution $x_s(t)$, instead of $r_s(t)$), are, from (3),

$$h_t - \beta\left(h^3 h_x\right)_x = 0 \tag{2.1a}$$

and

$$\int_0^{x_N(t)} h\,dx = A, \tag{2.1b}$$

indicating that there is a constant total area A associated with the flow. By definition, x_N also clearly satisfies the condition that $h(x_N) = 0$. We solve this with similarity variables as in (**3**). Start by taking

$$\eta = \left(\beta A^3\right)^{-1/5} x t^{1/5}. \tag{2.2}$$

Then, letting η_N be the value of η at x_N, with $y = \eta/\eta_N$, postulate a solution of the form

$$h(y,\ t) = \eta_N^{2/3}\left(A^2/\beta\right)^{1/5} t^{-1/5}\phi(y), \tag{2.3}$$

for some function ϕ that must satisfy

$$\frac{\partial}{\partial y}\left(\phi^3\frac{\partial\phi}{\partial y} + \frac{1}{5}y\phi\right) = 0. \tag{2.4}$$

Noting also that $\int_0^1 \phi\,\mathrm{d}y = 1$, we can solve for the constant η_N, and this leads to the similarity solution

$$x_s = \eta_N\left(\beta A^3\right)^{1/5} t^{1/5}, \tag{2.5}$$

resulting in a suggested equilibration time τ satisfying

$$A^{1/2}\beta\tau\gamma_0^{5/2} = p^{-1} f_a(p,\ \text{shape}), \tag{2.6}$$

as derived by (**2**), where f_a is some function of p, to be determined, relating equilibration time to percentage difference. For reasons that will become clear later, we take a factor of p^{-1} out in this case. Here, γ_0 is the aspect ratio of the initial shape, h_0/x_0. We plot numerical values of $x_N(t)$ and the similarity solution (2.5) above to first show the convergence of $x_s(t)$ to $x_N(t)$. In this case, we take the initial shape of fluid to be a square of side length 1, with vertices $(x,\ h) = (0,\ 0),\ (1,\ 0),\ (1,\ 1),\ (0,\ 1)$ (thus giving $\gamma_0 = 1$), with the results shown in Fig. 1. Equation (2.6) suggests that plots of $\ln\tau_{5\%}$ against $\ln\beta$ should give a straight line of gradient -1, and we can therefore confirm that $\tau \propto 1/\beta$, as well as confirming the numerical reliability of our program, as shown in Fig. 2. A similar approach holds to show the stated power-law dependence on γ_0 and A. Finally, it remains to seek a form for $f_a(p,\ \text{rectangle})$. Postulating a form $f_a(p,\ \text{rectangle}) = B\left[1 - \varepsilon p + \mathcal{O}\left(p^2\right)\right]$, and plotting $p\beta\tau_{p\%}$ (A and γ_0 are held constant at 1) against p in each case gives the same curve, which, for sufficiently small p, is approximately linear, giving

$$f_a(p,\ \text{rectangle}) \approx 5.9\left[1 - 0.017p + \mathcal{O}\left(p^2\right)\right], \tag{2.7}$$

as evidenced in Fig. 3. Therefore, we argue that, for sufficiently small p, the behaviour of τ is dominated by the $1/p$ term.

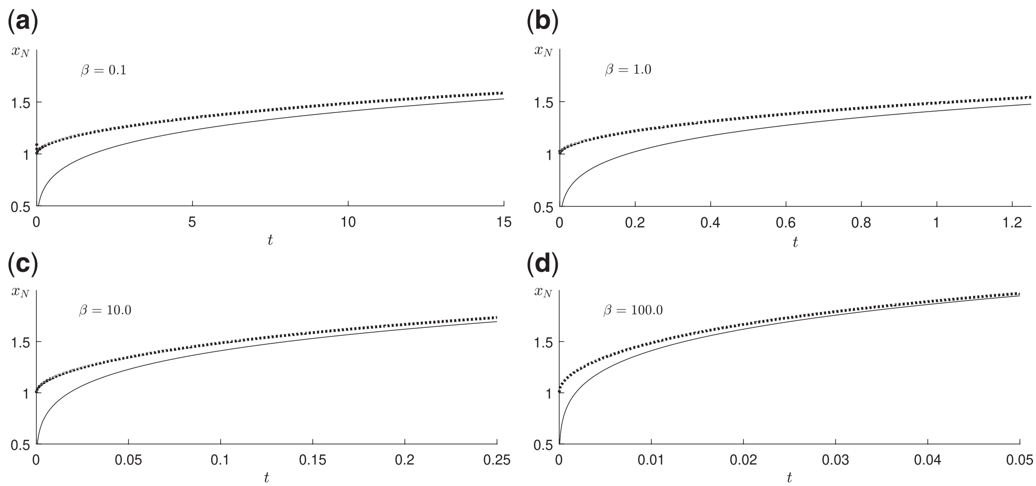

Fig. 1 Plots of the numerical solutions for x_N (dotted line) against time and the similarity solution x_s (solid line) for (2.1) with initial shape of a square of unit side length. Note the difference in timescales in each case.

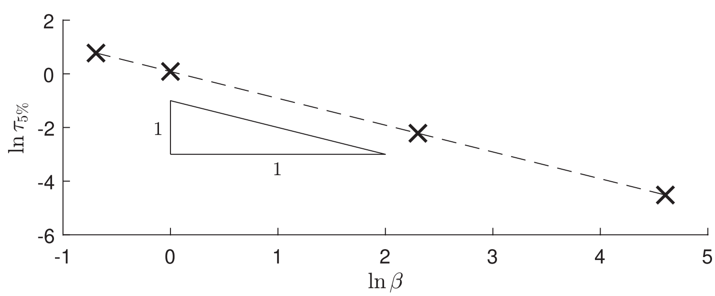

Fig. 2 A plot of $\ln \tau_{5\%}$ against $\ln \beta$ for the case described by (2.1). The numerically calculated best-fit line has a gradient of -0.9992.

It remains to determine expansions of $f_a\,(p,\ \text{shape})$ in the form $B\left[1 - \varepsilon p + \mathcal{O}\left(p^2\right)\right]$ for other shapes, the results of which are summarised in Table 1. We note that the values for ε here are mostly comparable to those found for (1.1) by (**2**) (with the corresponding three-dimensional (3D) axisymmetric shapes found by rotating these shapes around the axis, such that a square becomes a cylinder, etc.), and the values of B are around twice as large as in the aforementioned case, except for the case of the inverted triangle geometry, which appears to converge considerably more slowly, leading to a far greater value of B.

Investigating this further by introducing a new geometry, a ‘boxcar’ shape—as defined in Table 1—it can be seen that convergence is also slower in this case, and it becomes clear that under both this initial shape, and the inverted triangle geometry, there are significant amounts of ‘backwards’ flow (in the negative x direction). This greatly increases the amount of time taken to agree with the similarity

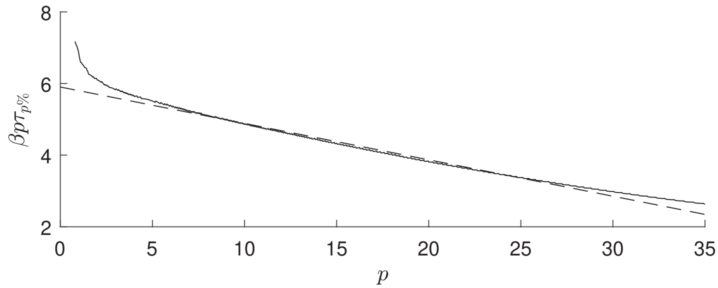

Fig. 3 A plot of $\beta p \tau_{p\%}$ against p to illustrate a first-order expansion for f_a (p, rectangle)—first-order approximation is shown by the dashed line. Note that the anomalous curvature of the line for very small p is due to round-off error in the numerical integration.

Table 1 A table of values of B and ε for solutions to (2.1) with different initial shapes

Initial shape	**B**	**ε**
Rectangle	5.9	0.017
Quarter-ellipse ($x^2/x_0^2 + h^2/h_0^2 = 1$)	5.2	0.016
Inverted triangle *(initial height zero for all $x > x_0$, otherwise $h_0 r/x_0$)*	116.0	0.023
Boxcar *(initial height zero for all $0 < x < 1$ and $x > x_0$, otherwise h_0)*	44.7	0.014

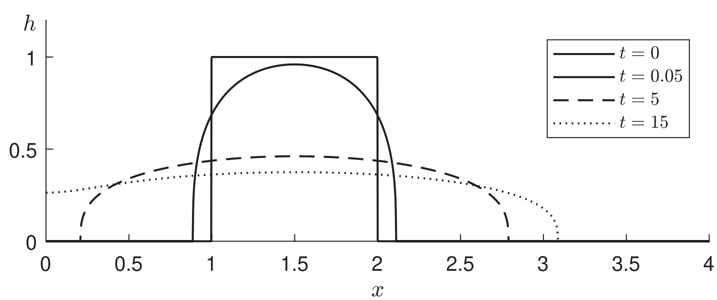

Fig. 4 A height profile for a boxcar shape, displaced from the origin, with $x_0 = 2$ and $h_0 = 1$, $\beta = 1$, showing how flow is not entirely unidirectional.

solution, and results in a larger overall magnitude of f_a. Observing a height plot of this boxcar shape (Fig. 4), shows this behaviour clearly - for early times in the flow considered here, there are equal amounts of flow in both directions, until the impenetrable barrier at $x = 0$ is reached. Therefore, for the early behaviour of the flow, the similarity solution best describing the radial extent of the flow would be that for a cylinder of initial radius $1/2$, offset by a radial distance of $3/2$, explaining why convergence to the actual similarity solution is considerably slower.

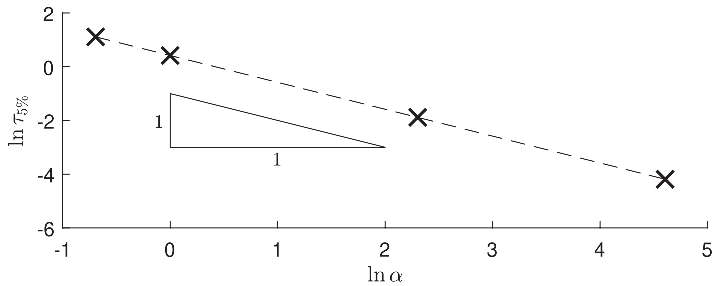

Fig. 5 A plot of $\ln \tau_{5\%}$ against $\ln \alpha$ for the case described by (2.8), with best-fit line of gradient -1.0000.

2.2 *A 2D gravity current in a porous medium*

In this case, from Phillips (**7**), the governing equation is

$$h_t - \alpha\,(hh_x)_x = 0; \tag{2.8}$$

for α a parameter dependent on permeability, porosity, viscosity and gravity (subject to certain assumptions on the properties of the porous medium, detailed in Huppert & Woods (**8**)), again subject to the constraint of a constant total area. The similarity solution, derived by (**8**), is

$$x_s\,(t) = (9A\alpha t)^{1/3}. \tag{2.9}$$

A similar analysis as before to find an equilibration time leads to the postulated result

$$\alpha A^{-1/2}\gamma_0^{3/2}\tau = p^{-1} f_b\,(p,\ \text{shape}). \tag{2.10}$$

As previously, taking the same initial square shape with unit side length at time $t = 0$, we verify this by plotting $\ln \tau_{5\%}$ against $\ln \alpha$ for values $\alpha = 0.5,\ 1,\ 10,\ 100$, which should again take a gradient of -1, as is shown in Fig. 5. We can similarly check dependence on the other parameters of the problem. Again, we seek a first-order approximation to $f_b\,(p,\ \text{rectangle})$. Using the same method as shown in Fig. 3, we deduce that

$$f_b\,(p,\ \text{rectangle}) \approx 8.0\left[1 - 0.011p + \mathcal{O}\left(p^2\right)\right]. \tag{2.11}$$

which also shows that $\tau \sim 1/p$ for sufficiently small p. As before, we determine B and ε for different initial geometries, as shown in Table 2. We again note in this case the greater values of B in the inverted triangle and boxcar geometries, but remark that this specific problem is affected much less strongly by such changes in geometry, with equilibration times only increasing by a factor of less than 10.

2.3 *An axisymmetric gravity current in a porous medium*

This flow is governed by

$$h_t - \frac{\alpha}{r}\,(rhh_r)_r = 0 \tag{2.12a}$$

Table 2 A table of values of B and ε for solutions to (2.8) with different initial shapes

Initial shape	**B**	$\boldsymbol{\varepsilon}$
Rectangle	8.0	0.011
Quarter-ellipse	7.4	0.010
Inverted triangle	44.7	0.014
Boxcar	60.0	0.016

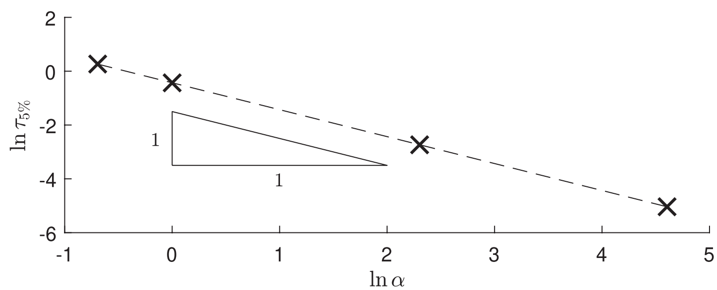

Fig. 6 A plot of $\ln \tau_{5\%}$ against $\ln \alpha$ for (2.12). The best-fit line has gradient -1.0005.

as derived by Lyle *et al.* (**9**), where α here again depends on the porosity, permeability, viscosity and gravity. Also,

$$2\pi \int_0^{r_N(t)} rh \, dr = V, \tag{2.12b}$$

where V is the total volume. Again, we introduce similarity variables to find the form of $r_s(t)$, as derived in (**9**)

$$r_s(t) = 2 (\alpha V/\pi)^{1/4} t^{1/4} \tag{2.13}$$

and then, in the same way as above, solve for the purported relation

$$\tau = \left(V/\gamma_0^4\right)^{1/3} (\alpha p)^{-1} f_c(p, \text{ shape}). \tag{2.14}$$

We take initial conditions of a solid cylinder of radius 1 and height 1, and plot, in Fig. 6, $\ln \tau_{5\%}$ against $\ln \alpha$ with $\alpha = 0.5, 1, 10, 100$. This again confirms a dependence on α^{-1}. Finally, we determine an approximate form for $f_c(p, \text{ cylinder})$, the axisymmetric 3D analogue of the rectangle used in sections 2.1 and 2.2. Again using the same technique, plotting $\pi^{-1/3}\alpha p \tau_{p\%}$ against p (because $\gamma_0 = 1$ and $V = \pi$ in this specific case), we determine that

$$f_c(p, \text{ cylinder}) \approx 2.5 \left[1 - 0.018p + \mathcal{O}\left(p^2\right)\right]. \tag{2.15}$$

Changing the geometry of the problem, by choosing the solids of revolution formed by the examples in sections 2.1 and 2.2, we find the results in Table 3. This table again shows slower equilibration for the final two geometries, when compared with the first two, but with a weaker effect than in sections 2.1 or 2.2 (equilibration times only increase by a factor of approximately 2.5 in this case).

Table 3 A table of values of B and ε for solutions to (2.12) with different initial shapes

Initial shape	**B**	$\boldsymbol{\varepsilon}$
Circular cylinder	2.5	0.018
Ellipsoid	2.6	0.014
Inverted cone	6.5	0.024
Cylindrical ring *(initial height h_0 for $1 < r < r_0$, and otherwise zero)*	6.3	0.026

3. The shallow-water equations

Having discussed the above cases, where convergence to the similarity solution was strictly monotonic, and thus the suppositions of (**2**) could be applied directly to the problem, we now investigate these suppositions in cases where the convergence to the similarity solution may not be as straightforward. We do this by considering the (one-layer) shallow-water equations, which describe the dynamics of high-Reynolds-number gravity currents in cases where either a thin and relatively light fluid layer intrudes above a heavier fluid layer, or a thin and relatively heavy fluid layer intrudes underneath a lighter fluid layer. In either case, the layer in question needs to have a thickness small compared with both its length (x_N or r_N in earlier sections) and the thickness of the other fluid comprising the system – more details are discussed in Simpson (**10**) and Ungarish (**11**). In the context of this article, we will only consider currents obeying the Boussinesq approximation.

For our purposes, we begin by considering a relatively heavy 2D current intruding above an impenetrable base under a lighter fluid (discussion of an axisymmetric current is reserved for section 3.3). We also take the height of our gravity current to be negligible compared with the height of the lighter fluid layer. As stated in (**6**), and elsewhere, the equations governing such a current are

$$\frac{\partial h}{\partial t} + u\frac{\partial h}{\partial x} + h\frac{\partial u}{\partial x} = 0 \tag{3.1a}$$

and

$$\frac{\partial u}{\partial t} + u\frac{\partial u}{\partial x} + g'\frac{\partial h}{\partial x} = 0, \tag{3.1b}$$

where $u\,(x,\ t)$ is the speed of the flow parallel to its base, and

$$g' = g\left(\rho_{\text{heavier}} - \rho_{\text{lighter}}\right)/\rho_{\text{heavier}}. \tag{3.2}$$

Additionally, we impose the boundary and initial conditions

$$u\,(0,\ t) = 0, \tag{3.3a}$$

$$u\,(x_N,\ t) = \dot{x}_N, \tag{3.3b}$$

$$u\,(x,\ 0) = 0, \tag{3.3c}$$

$$\dot{x}_N^2 = \mathrm{Fr}^2\, g' h\,(x_N,\ t), \tag{3.3d}$$

$$h\,(x,\ 0) = \begin{cases} h_0 & 0 \le x \le x_0 \\ 0 & x_0 < x \end{cases} \tag{3.3e}$$

for constants h_0, x_0 and Fr—see Appendix A for more details on the value of Fr, the Froude number. We also impose the condition that the volume per unit width of the denser fluid is conserved, with a constant value V [just as in (2.1)]. Grundy and Rottman, in (6), repeat the similarity solution

$$x_s(t) = A_0 \left(g'V\right)^{1/3} t^{2/3}, \tag{3.4}$$

originally derived in (4). In our case, the constant $A_0 \approx 1.39$ (more detail on this derivation is presented in Appendix A).

3.1 *Comparing $x_N(t)$ to $x_s(t)$*

3.1.1 Numerical solution. To solve this system numerically, we use an approach based on that posed by the authors of Bonnecaze *et al.* (12) and (11). Letting $y = x/x_N$ and $T = t$, the shallow-water equations (3.1) become

$$\frac{\partial h}{\partial T} = \frac{1}{x_N}\left\{(y\dot{x}_N - u)\frac{\partial h}{\partial y} - h\frac{\partial u}{\partial y}\right\}, \tag{3.5a}$$

$$\frac{\partial u}{\partial T} = \frac{1}{x_N}\left\{(y\dot{x}_N - u)\frac{\partial u}{\partial y} - g'\frac{\partial h}{\partial y}\right\}. \tag{3.5b}$$

We then transform the boundary and initial conditions of (3.3) into this new system, detailed in (3.6). Unlike in (12), which uses a two-step Lax–Wendroff approach, we solve these equations numerically with a Lax–Friedrichs approach, for a y-domain of $[0,\ 1]$. Values at the endpoints $y = 0$ and $y = 1$ are determined through the boundary conditions and through finite-difference representations of (3.5).

$$u(0,\ T) = 0, \tag{3.6a}$$

$$u(1,\ T) = \dot{x}_N, \tag{3.6b}$$

$$u(y,\ 0) = 0, \tag{3.6c}$$

$$\dot{x}_N^2 = \mathrm{Fr}^2 g'h(1,\ T), \tag{3.6d}$$

$$h(y,\ 0) = h_0. \tag{3.6e}$$

3.1.2 Convergence to the similarity solution. Grundy and Rottman (6) indicate that convergence of the numerical solution of the shallow-water equations to the similarity solution stated as (3.4) is oscillatory in nature. Producing a plot of p against $\ln t$ (to better show the long timescales involved), we confirm that this is indeed the case. The plot in Fig. 7 clearly shows that the percentage difference between x_N and x_s is monotonically decreasing up to some time $t = t_*$, before increasing again. The similarity solution x_s then goes on to converge in an oscillatory manner, with properties described in more detail by (6). We will show that the methods of (2) apply in the initial period $0 \le t < t_*$, when convergence is still monotonic.

3.1.3 Dependence of τ on the parameters of the problem. Noting that the only dimensional quantities on which this system depends are V and g', with dimensions L^2 and LT^{-2}, respectively, we could postulate that $\tau \propto \left(V/g'^2\right)^{1/4}$, using the same approach as the problems in section 2.

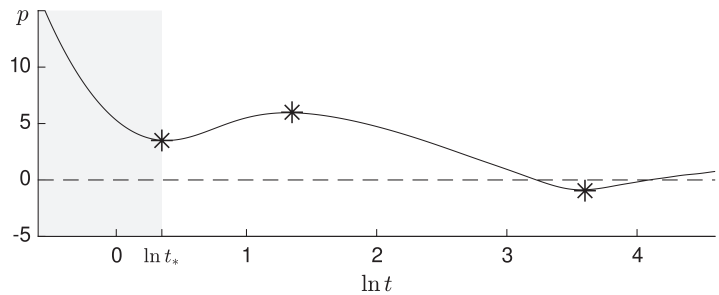

Fig. 7 A plot of the percentage difference p between x_N and x_s over time – note the local minimum at t_*, and the subsequent extrema, marked by asterisks on the plot. This plot is smoothed to remove slight oscillations as time increases and rounding errors begin to affect the results. The shaded region shows where convergence is monotonic.

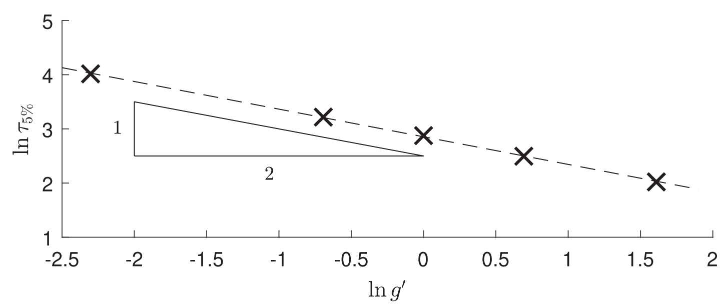

Fig. 8 A plot of $\ln \tau_{5\%}$ against $\ln g'$ for the shallow-water equations (3.1). The calculated best-fit line (shown as a dashed line) has a gradient $-0.5099 \approx -1/2$.

However, our initial numerical results indicated that this was not the case, and a different approach was sought.

To show why this is, consider the only timescale of the equation, up to a multiplicative constant,

$$\sigma = x_0 \left(h_0 g'\right)^{-1/2} \tag{3.7}$$

and note that we cannot eliminate x_0 and h_0 through combinations of $V = x_0 h_0$ and $\gamma_0 = h_0/x_0$, so τ must depend explicitly on x_0 and h_0 separately, completely unlike the cases in section 2.

We plot values of $\ln \tau_{5\%}$ against $\ln g'$ (Fig. 8), $\ln x_0$ (Fig. 9) and $\ln h_0$ (Fig. 10) to confirm the conclusions implicit from (3.7).

Naturally, errors propagating in the numerical solutions mean that the gradients inferred numerically from the graphs do not match the theoretical values exactly. The deviation is greater than that for the cases in section 2 due to a combination of factors, not least shocks arising in the solution of (3.1) [discussed by (**12**) in more depth] and the fact that our choice of Fr is merely an approximation.

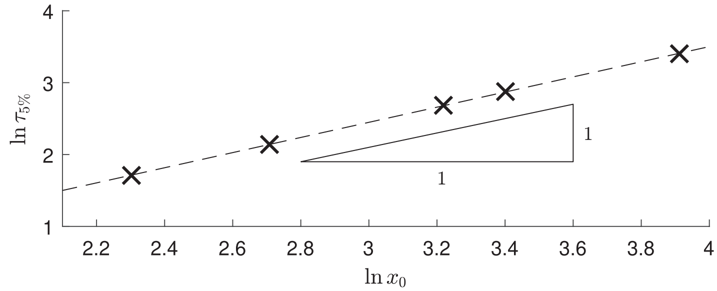

Fig. 9 A plot of $\ln \tau_{5\%}$ against $\ln x_0$ for the shallow-water equations (3.1). The calculated best-fit line has a gradient of $1.0533 \approx 1$.

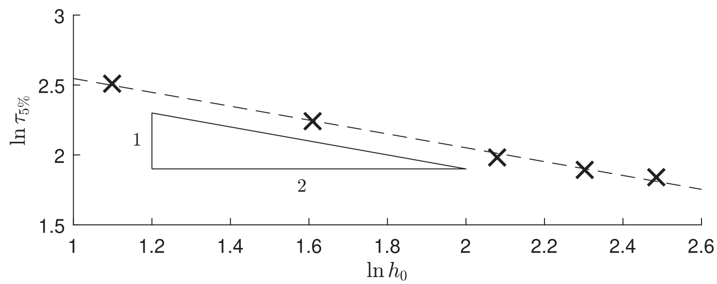

Fig. 10 A plot of $\ln \tau_{5\%}$ against $\ln h_0$ for the shallow-water equations (3.1). The best-fit line has a gradient of $-0.4955 \approx -1/2$. This behaviour is only shown for a relatively narrow range of h_0 – it was found that for values of $\gamma_0 = h_0/x_0$ much greater than 1, the relationship no longer holds, probably because the problem is not well-modelled by the shallow-water equations.

A similar analysis to the above shows that τ is proportional to $(\mathrm{Fr})^{-3}$, shown in Fig. 11. However, for most purposes, we will simply take $\mathrm{Fr} = 1$ – this is not a parameter to vary in the same way that the other involved parameters are, because it is instead a property of the flow itself. As stated in Appendix A, the authors of (**6**) take $\mathrm{Fr} = 1$ in their analysis of the problem.

Therefore, we know that τ is proportional to $x_0 \left(g'h_0\right)^{-1/2} \mathrm{Fr}^{-3}$ in this 2D case, with some other dependence, to be determined, on the shape and percentage difference p. Note here that we are no longer making the supposition that this relationship is dominated by a p^{-1} term, as was the case beforehand.

$$\tau_{p\%} = x_0 \left(g'h_0\right)^{-1/2} \mathrm{Fr}^{-3} f\,(p,\ \text{shape}). \tag{3.8}$$

3.1.4 Seeking the form of $f\,(p,\ \text{shape})$. Again, working only for times $0 \leq t < t_*$, we seek a form of the function $f\,(p,\ \text{shape})$, and start by considering whether τ decreases as $1/p$ (as was the case for the problems in section 2), or in some other manner.

It is important to remark that we are restricting our attention to the first phase of (monotonic) convergence here, the shaded region on Fig. 7—$\tau_{p\%}$ represents the time at which the solutions first agree to within $p\%$, for $p > p_{\min}$, the value of p at time t_*.

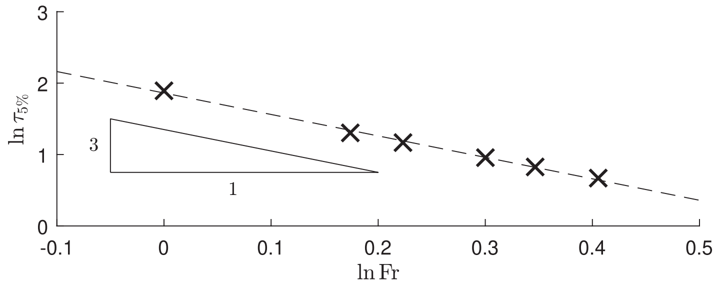

Fig. 11 A plot of $\ln \tau_{5\%}$ against $\ln \mathrm{Fr}$ for the shallow-water equations (3.1). The best-fit line has gradient -3.0042.

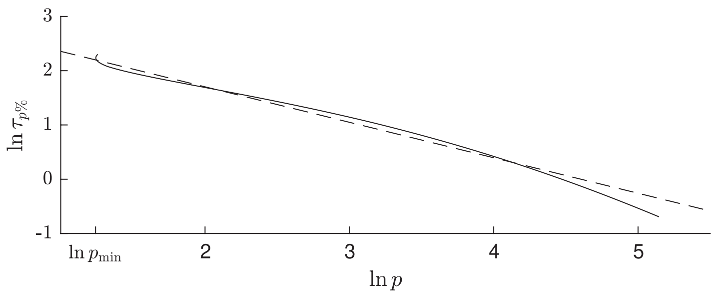

Fig. 12 A plot of $\ln \tau_{p\%}$ against $\ln p$ demonstrating that, for many values of p, τ is approximately proportional to $p^{-2/3}$ – the best-fit line here has gradient $-0.6538 \approx -2/3$.

A plot of $\ln \tau_{p\%}$ against $\ln p$ (Fig. 12) shows that, unlike the cases in section 2, convergence time is dominated by a $p^{-2/3}$ term, but that, in general, we can't apply a power law relationship in this case. This is perhaps illustrated more strongly if, for $0 \leq t < t_*$, we postulate that $f(p,\ \text{shape}) = p^{-2/3} f_d(p,\ \text{shape})$ for some function f_d, dependent on the initial shape and p. We then remark that $f_d(p,\ \text{shape}) = p^{2/3} \tau_{p\%} \left(g' h_0\right)^{1/2} / x_0$, and so seek a linear approximation to f_d for small p, as we did in section 2. This plot in Fig. 13 shows that we cannot apply the same reasoning as before—there is no linear behaviour for small p, suggesting that $f(p,\ \text{shape})$ can't have an analogous form to the cases in section 2. The approximation by a power of p is seen to break down close to the local minimum at t_*.

If we interpret to the analysis of the authors of (**6**), it is seen that

$$x_N(t) = A_0 \left(g' V\right)^{1/3} t^{2/3} \left[1 + \sum_j \exp\left[\mathrm{Re}\left(\gamma_j\right) A_0 T\right] \left\{a_j \cos\left[\mathrm{Im}\left(\gamma_j\right) A_0 T\right] + b_j \sin\left[\mathrm{Im}\left(\gamma_j\right) A_0 T\right]\right\}\right], \tag{3.9}$$

where $T = \ln\left[\left(g' V\right)^{1/2} x_0^{-3/2} t\right] / A_0$ and γ_j are eigenvalues to be determined. The constants a_j and b_j also remain undetermined, but this form alone shows that convergence should be oscillatory in

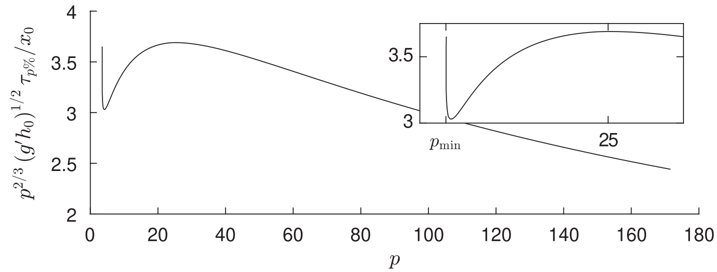

Fig. 13 A plot of $f_d\,(p,\ \text{cylinder})$ against p.

nature. From (3.9), it can also be seen that

$$p = 100 \sum_j \exp\left[\operatorname{Re}\left(\gamma_j\right) A_0 T\right] \left\{a_j \cos\left[\operatorname{Im}\left(\gamma_j\right) A_0 T\right] + b_j \sin\left[\operatorname{Im}\left(\gamma_j\right) A_0 T\right]\right\}. \tag{3.10}$$

It is shown in (**6**) that one of the eigenvalues, which we will call γ_0, is always equal to -1, and that all of the other eigenvalues have real part $-1/2$. Therefore, we rewrite our expression as

$$\begin{aligned} p = {} & 100 a_0 \left(g'V\right)^{-1/2} x_0^{3/2} t^{-1} \\ & + 100 \left(g'V\right)^{-1/4} x_0^{3/4} t^{-1/2} \underbrace{\sum_{j \neq 0} \left\{a_j \cos\left[\operatorname{Im}\left(\gamma_j\right) A_0 T\right] + b_j \sin\left[\operatorname{Im}\left(\gamma_j\right) A_0 T\right]\right\}}_{W(T)}. \end{aligned} \tag{3.11}$$

Letting $q = \left(g'V\right)^{-1/4} x_0^{3/4} t^{-1/2} = \left(g'h_0\right)^{-1/4} x_0^{1/2} t^{-1/2}$, it is seen that

$$a_0 q^2 + W\,(T)\,q - \frac{p}{100} = 0. \tag{3.12}$$

However, (3.8) suggests that q has no time-dependence, at least in the region of convergence we are considering. Therefore, assuming that $W\,(T)$ is approximately equal to some constant W_0, we can solve to find that

$$\tau_{p\%} = x_0 \left(g'h_0\right)^{-1/2} \mathrm{Fr}^{-3} \left(\frac{2\,\mathrm{Fr}^{3/2}\, a_0}{-W_0 \pm \sqrt{W_0^2 + \frac{a_0 p}{25}}}\right)^2. \tag{3.13}$$

As we expect $\tau_{p\%} \to \infty$ as $p \to 0$, we must pick the $+$ in $\pm$, and are therefore left with the postulated expression

$$f\,(p,\ \text{shape}) = \left(\frac{2\,\mathrm{Fr}^{3/2}\, a_0}{-W_0 + \sqrt{W_0^2 + \frac{a_0 p}{25}}}\right)^2. \tag{3.14}$$

This prediction can be matched with our numerical results, finding that, in the case of initially rectangular geometry, $a_0 \approx 0.375$ and $W_0 \approx -0.175$—Fig. 14 shows very strong agreement of this postulated form in the early period of convergence.

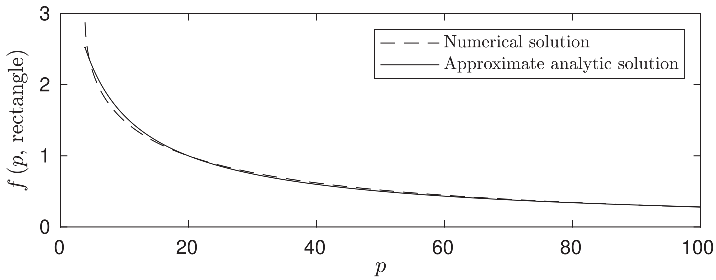

Fig. 14 A plot comparing the postulated form of $f(p, \text{cylinder})$ from (3.14) with numerical results from solving the shallow-water equations, showing very strong agreement.

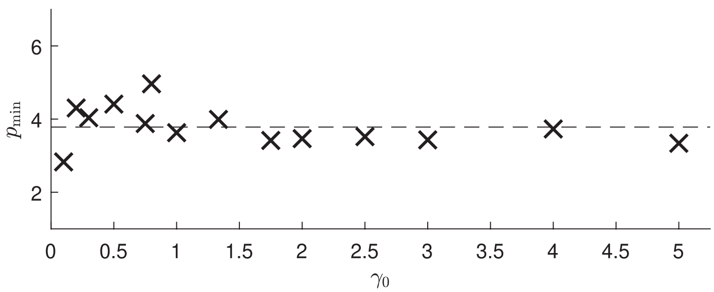

Fig. 15 A plot of $p_{\min}$ against γ_0, showing little variation (note the scale on the vertical axis).

3.1.5 Values of p at $t = t_*$. It is a natural development to consider the local minimum percentage difference at t_*, $p_{\min}$, and how this is affected by the problem in question. The only factors which could affect it are g', x_0 and h_0, as well as the Froude number Fr, but $p_{\min}$ is dimensionless, so it can only depend on $\gamma_0 = h_0/x_0$ and Fr – we can make no dimensionless group including other parameters.

Varying γ_0 in different cases, rather surprisingly, has very little effect on the value of $p_{\min}$, as shown in Fig. 15, and therefore this can be considered constant for any given initial shape, independent of dimensions, volume or g'.

Changing the value of Fr, however, including to the values suggested by other authors, shows a strong linear correlation. Numerical results suggest that $p_{\min} \approx 40\,(1 - 0.9\,\mathrm{Fr})$, as evidenced by the plot in Fig. 16, indicating that $p_{\min} \lessgtr 0$ for $\mathrm{Fr} \gtrless 1.095$. We illustrate a case where $p_{\min} < 0$, with for $\mathrm{Fr} = 1.19$, in Fig. 17.

3.2 *Convergence for $t > t_*$*

We now move on to consider the pattern of convergence for times beyond the local minimum at $t = t_*$, and seek to determine whether the approach of (2) can still be successfully applied. We consider values of $\tau_{0\%}$, the first time at which $x_N(t)$ is equal to $x_s(t)$, and postulate that $\tau_{0\%} \propto x_0 \left(g'h_0\right)^{-1/2}$, as we would conclude from dimensional analysis. Plots for $\ln \tau_{0\%}$ against $\ln g'$, $\ln x_0$ and $\ln h_0$ show

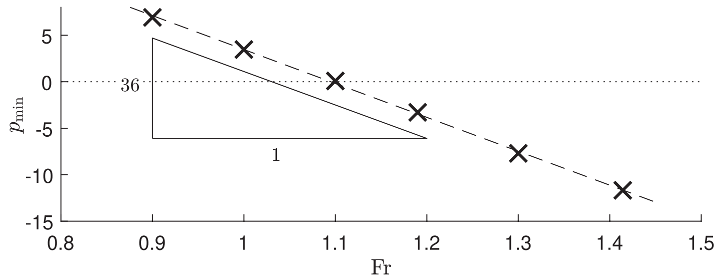

Fig. 16 A plot of p_{min} against Fr, showing an approximately linear relationship.

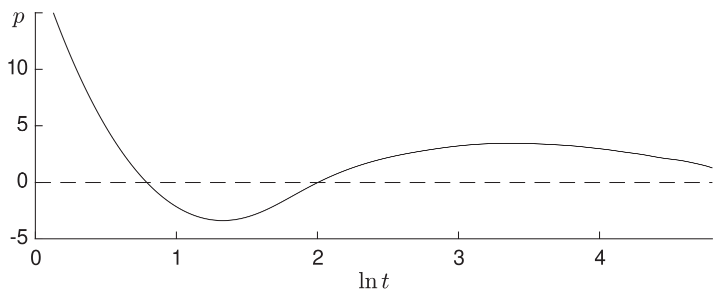

Fig. 17 A plot of p against $\ln t$ with $\text{Fr} = 1.19$ to show a negative value of p_{min}. This plot is smoothed to remove slight oscillations as time increases and rounding errors affect results.

that this is the case, as shown in Figs. 18–20. There are some deviations from the predicted values, because timescales are far larger, providing a greater opportunity for error in the numerical solution to affect the results.

Thus we can state that, taking rounding error into account, for the 2D shallow-water equations,

$$\tau_{p\%} = x_0 \left(g' h_0\right)^{-1/2} \text{Fr}^{-3} f\,(p,\ \text{shape}), \tag{3.15}$$

where $f\,(p,\ \text{shape})$ is a potentially discontinuous function. This is to account for the discontinuity arising in $\tau_{p\%}$ at $p = p_{\text{min}}$. For example, in the case illustrated in Fig. 7, $\tau_{p_{\text{min}\%}} = t_* < 2$ but $\tau_{(p_{\text{min}}-\epsilon)\%} > 8$ for all $\epsilon > 0$, by inspection.

3.3 *Axisymmetric case*

The governing equations for the axisymmetric analogue of the problem discussed in section 3 are, from (**6**),

$$\frac{\partial h}{\partial t} + u\frac{\partial h}{\partial r} + h\frac{\partial u}{\partial r} + \frac{uh}{r} = 0 \tag{3.16a}$$

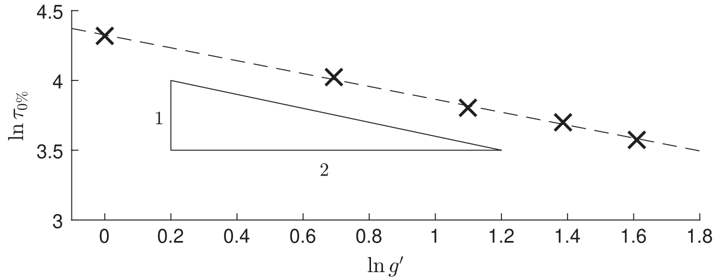

Fig. 18 A plot of $\ln \tau_{0\%}$ against $\ln g'$ for the shallow-water equations (3.1). The calculated best-fit line (shown as a dashed line) has a gradient -0.4617. There is some deviation from the theoretical value of $-1/2$ due to the long timescales involved.

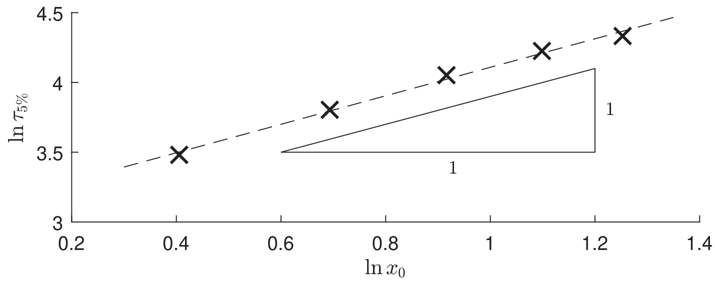

Fig. 19 A plot of $\ln \tau_{0\%}$ against $\ln x_0$ for the shallow-water equations (3.1). The calculated best-fit line has a gradient of $1.0210 \approx 1$, again with some deviation due to rounding error over time.

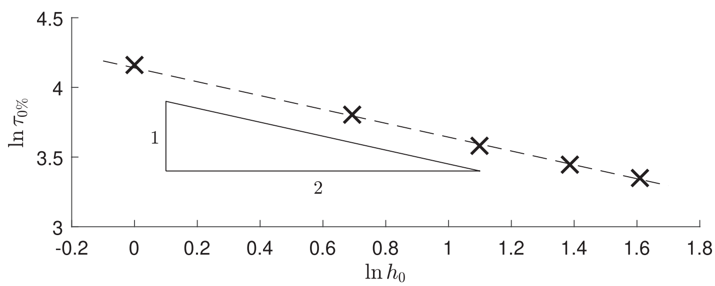

Fig. 20 A plot of $\ln \tau_{0\%}$ against $\ln h_0$ for the shallow-water equations (3.1). The best-fit line here has gradient $-0.4973 \approx -1/2$.

and

$$\frac{\partial u}{\partial t} + u\frac{\partial u}{\partial r} + g'\frac{\partial h}{\partial r} = 0, \tag{3.16b}$$

subject to

$$u(0,\ t) = 0, \tag{3.17a}$$

$$u(r_N,\ t) = \dot{r}_N, \tag{3.17b}$$

$$u(r,\ 0) = 0, \tag{3.17c}$$

$$\dot{r}_N^2 = \mathrm{Fr}^2\, g' h(r_N,\ t), \tag{3.17d}$$

$$h(r,\ 0) = \begin{cases} h_0 & 0 \le r \le r_0 \\ 0 & r_0 < r \end{cases} \tag{3.17e}$$

Here, the similarity solution is

$$r_s(t) = A_0 \left(g'V\right)^{1/4} t^{1/2}, \tag{3.18}$$

for V the total fluid volume and, in this case, $A_0 \approx 1.14$ (see Appendix A).

Identical analysis to the above shows that $\tau_{p\%} = \left(g'^3 \gamma_0^4 / V\right)^{-1/6} f(p,\ \text{shape})$, for V the total volume of the current and $\gamma_0 = h_0/r_0$. Unlike the 2D case, this only depends on the aspect ratio of the original shape and not on its specific dimensions r_0 and h_0. This might be unsurprising given the different shape of the current; specifically that the current head, in the axisymmetric case (**3**), is very different to that in two dimensions.

4. Time-shifted similarity solutions

In all of the cases described above, it is clear that the similarity solutions $x_s(t)$ (or r_s in axisymmetric cases) all have $x_s(0) = 0$, and so the percentage disagreement with x_N is initially boundlessly large. The authors of (**2**) introduce a method for 'time-shifting' the similarity solution such that we instead consider $x_s(t + t_0)$ or $r_s(t + t_0)$ where t_0 is some time such that $x_s(t_0) = x_0$ or $r_s(t_0) = r_0$.

4.1 *Time-shifting in a monotonic case*

Considering (2.1) above, we seek a time t_0 where $x_s(t_0) = x_0$. Taking $x_0 = 1$, this can be seen to be given by

$$t_0 = \left(\beta A^3 \eta_N^5\right)^{-1}. \tag{4.1}$$

Then, taking the similarity solution $x_s = \eta_N (\beta A^3)^{1/5} (t + t_0)^{1/5}$, we have a solution which agrees with the numerical result faster. This is evidenced by the plots in Fig. 21—the percentage difference appears less in this shifted case at all observed times.

Analogous forms of t_0 for all of the other canonical cases described in section 2 are listed in Table 4.

4.1.1 Maximum percentage difference. The plots in Fig. 21 clearly show that the percentage difference between $x_s(t + t_0)$ and $x_N(t)$ reaches a maximum value—as was the case with the minimum value $p_{\min}$ at t_* for the shallow-water equations. Indeed, this would be expected, as the initial percentage difference is zero, and the percentage difference tends to zero as $t \to \infty$, and thus we seek an expression for $p_{\max}$. This could depend on any of the parameters of the problem, but again, a dimensional argument rules out all of them but γ_0.

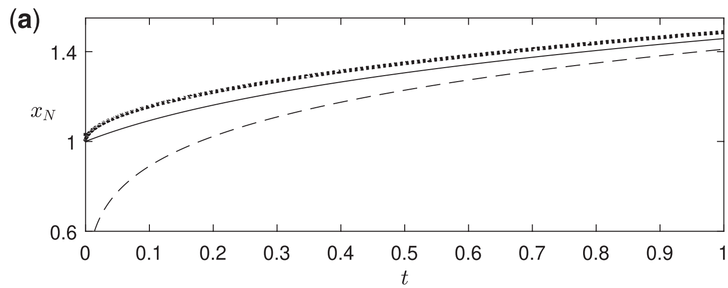

A plot of the numerical solution (dotted line), $x_s(t)$ (dashed line) and $x_s(t+t_0)$ (solid line).

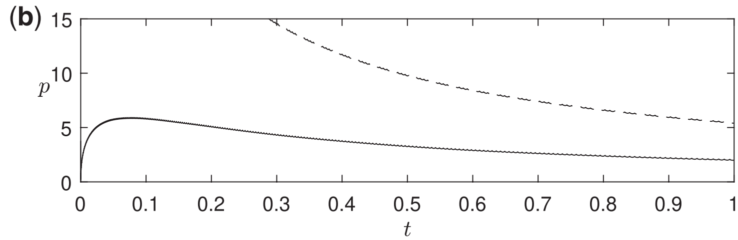

A plot of the percentage difference between $x_N(t)$ and $x_s(t)$ (dashed line) and between $x_N(t)$ and $x_s(t+t_0)$.

Fig. 21 Revisiting the case of (2.1) with $\beta = 1$, showing that the time-shifted similarity solution is a better approximator of $x_N(t)$.

Table 4 Values of t_0 for different problems outlined in section 2

Case	**Form of t_0**
2D viscous (section 2.1)	$(\beta A^3)^{-1}(x_0/\eta_N)^5$
2D in porous medium (section 2.2)	$x_0^3/(9A\alpha)$
Axisymmetric in porous medium (section 2.3)	$\pi r_0^4/(16\alpha W)$

Again we find that changing γ_0 makes no difference to the value of this maximum, which remains constant at around 5.9%. This maximum percentage difference is found to be independent of parameters and initial dimensions, but a function only of the initial shape. These values are shown for different problems and geometries in Table 5.

It is also instructive to consider the amount of time taken to reach this maximum value—naturally, by a dimensional argument, we can argue, via a similar approach to that used to derive (2.6), that this should take the form

$$t_{\max} = T_1 \beta^{-1} A^{-1/2} \gamma_0^{-5/2}, \tag{4.2}$$

for T_1 a dimensionless constant to be determined. This can easily be verified numerically by considering the plots in Fig. 22, and the value of T_1, which is postulated to depend on initial geometry, can also be found by a similar approach, as in Table 6.

Table 5 Maximum percentage differences between $r_s\,(t + t_0)$ and $r_N\,(t)$ for the problems discussed in section 2, with different initial geometries

Shape	**2D viscous (%)**	**2D in porous medium (%)**	**Axisymmetric in porous medium (%)**
Rectangle/cylinder	5.94	13.00	9.76
Quarter-ellipse/ellipsoid	2.42	5.58	4.32
Inverted triangle/cone	17.59	21.15	12.92
Boxcar/ring	23.06	23.99	12.83

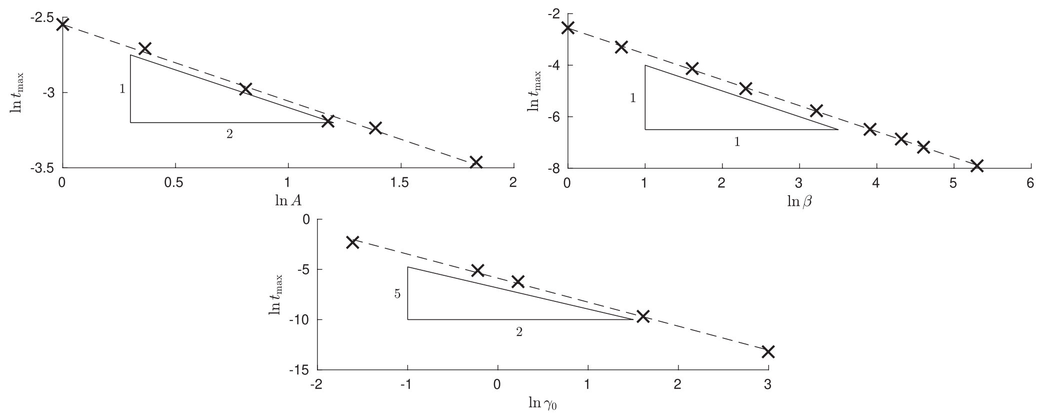

Fig. 22 Log–log plots showing the validity of the model in (4.2) for the time taken to approach maximum percentage difference from the time-shifted similarity solution in the case of an initially rectangular geometry, for a 2D viscous gravity current.

Table 6 Values of T_1 for different initial geometries and for the different problems in section 2, where T_1 is defined analogously to its definition in (4.2) in all cases

Shape	**2D viscous**	**2D in porous medium**	**Axisymmetric in porous medium**
Rectangle/cylinder	0.07823	0.05911	0.03374
Quarter-ellipse/ellipsoid	0.09735	0.06584	0.04773
Inverted triangle/cone	0.00001	0.09971	0.09978
Boxcar/ring	0.09962	0.09976	0.09970

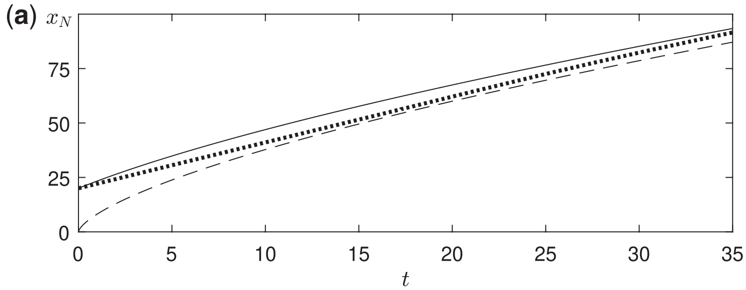

A plot of the numerical solution $x_N(t)$ (dotted line), $x_s(t)$ (dashed line) and $x_s(t+t_0)$ (solid line).

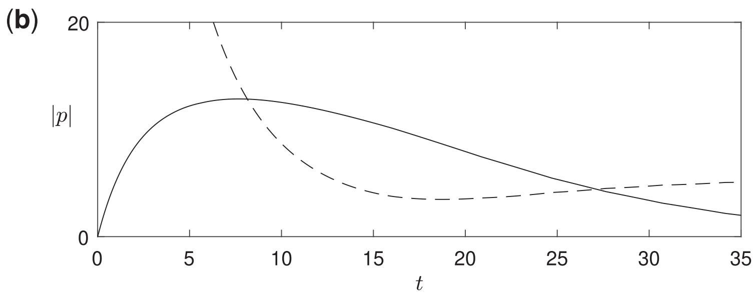

A plot of percentage differences between $x_s(t)$ and $x_N(t)$ (dashed line) and between $x_s(t+t_0)$ and $x_N(t)$ (solid line).

Fig. 23 Plots for the similarity solution (dashed line) and time-shifted similarity solution (solid line) with the shallow-water equations (3.1), using initial conditions of a circular cylinder, $x_0 = 20$, $h_0 = 10$ and $g' = 1$.

4.2 *Time-shifting for the shallow-water equations*

We proceed initially in the same manner as for the canonical cases above, seeking some t_0 such that

$$A_0 \left(g'V\right)^{1/3} t_0^{2/3} = x_0; \tag{4.3}$$

so we take $t_0 = x_0^{3/2} / \left(A_0^3 g'V\right)^{1/2}$. Plotting both the original similarity solution and this new, shifted, solution on the same graph shows that, in this case, the shifted solution very quickly becomes a worse approximation to the actual behaviour. This is not unexpected; the work of (6) and our own confirmation of these results shows that there is some time at which the percentage difference between $x_s(t)$ and $x_N(t)$ is zero, where clearly the percentage difference between $x_s(t+t_0)$ and $x_N(t)$ is greater in magnitude than this.

Thus there is no discernible benefit in choosing the time-shifted solution in non-monotonic cases like this, at least beyond the initial time period of monotonic convergence ($0 < t < t_*$), where the reasoning in section 4.1.1 can be applied.

5. Conclusions

We have shown that equilibration times for various gravity currents—the timescales over which the furthest radial extent of the current agrees with a similarity solution—can be found by dimensional analysis of the parameters involved in the current. This approach has been shown to apply equally well if we allow the expressions for equilibration time to be discontinuous in p, where predictions for equilibration times can be extended to any period of monotonic convergence for high-Reynolds-number flows, even after periods during which the similarity solution grows away from the numerical solution.

This shows that the methods outlined in (**2**) can be applied to a wide variety of situations where the radial (or, in the 2D case, horizontal) extent of a gravity current approaches a similarity solution over time both monotonically and non-monotonically. With appropriate modifications for the situation in hand, the predictions given by this approach agree very closely with solutions obtained via a numerical approach. However, unlike in (**2**), and the current described by (1.1), it is seen that equilibration time depends explicitly on the dimensions of the initial mass of fluid, and not simply on the shape of the initial fluid. We are also able to reconcile the analytical discussion of convergence by Grundy and Rottman (**6**) with our numerical results, noting that convergence to the similarity solution no longer occurs on a timescale approximately proportional to a power of the percentage difference p. It remains an open question as to whether these methods can be applied to gravity currents where the Boussinesq approximation is not made—Ungarish and Zemach (**13**) detail an example where a similarity solution exists, but the gravity current propagates axisymmetrically in a ring shape after some time.

Furthermore, we note that, by considering different cases as in section 2, the dependence of equilibration times on different initial geometries is somewhat different—the effect of backflow on how quickly we approach the similarity solution differs greatly when considering different equations; the reasons behind this are a potential source of further research.

We have also detailed an approach for time-shifting similarity solutions such that their initial value agrees with the initial radial extent of a gravity current, and shown that this time-shifted case has certain properties making it more desirable for use than the normal similarity solution. It is seen that the percentage difference between the numerical solution and the time-shifted similarity solution is bounded above by a value dependent only on the initial shape, and we note that the time taken to reach this maximum has the same dependence on the parameters of the problem as the equilibration time. Such time-shifting, however, is shown to be undesirable in cases where the convergence to the similarity solution is not monotonic, such as high-Reynolds-number flow.

Acknowledgements

We thank John Hinch for his, as usual, stimulating input on the numerical solution of the shallow-water equations, and John Lister who wrote original versions of the program which was modified to solve the problems in section 2. We also thank Thomasina Ball, who adapted this program and answered questions on its usage. Joseph Webber is thankful for the financial support of the Heilbronn Fund at Trinity College.

References

1. H. E. Huppert, Gravity currents: a personal perspective, *J. Fluid Mech.* **554** (2006) 299–322.
2. T. V. Ball and H. E. Huppert, Similarity solutions and gravity current adjustment times, *J. Fluid Mech.* **874** (2019) 285–298.
3. H. E. Huppert, The propagation of two-dimensional and axisymmetric viscous gravity currents over a rigid horizontal surface, *J. Fluid Mech.* **121** (1982) 43–58.

4. D. P. Hoult, Oil spreading on the sea, *Ann. Rev. Fluid Mech.* **4** (1972) 341–368.
5. H. E. Huppert and J. E. Simpson, The slumping of gravity currents, *J. Fluid Mech.* **99** (1980) 785–799.
6. R. E. Grundy and J. W. Rottman, The approach to self-similarity of the solutions of the shallow-water equations representing gravity-current releases, *J. Fluid Mech.* **158** (1985) 39–53.
7. O. M. Phillips, *Flow and Reactions in Permeable Rocks* (Cambridge University Press, Cambridge 1991).
8. H. E. Huppert and A. W. Woods, Gravity-driven flows in porous layers, *J. Fluid Mech.* **292** (1995) 55–69.
9. S. Lyle, H. E. Huppert, M. Hallworth, M. Bickle and A. Chadwick, Axisymmetric gravity currents in a porous medium, *J. Fluid. Mech.* **543** (2005) 293–302.
10. J. E. Simpson, *Gravity Currents: In the Environment and the Laboratory*, 2nd edn. (Cambridge University Press, Cambridge 1999).
11. M. Ungarish, *An Introduction to Gravity Currents and Intrusions* (CRC Press, Boca Raton, FL 2009).
12. R. T. Bonnecaze, H. E. Huppert and J. R. Lister, Particle-driven gravity currents, *J. Fluid Mech.* **250** (1993) 339–369.
13. M. Ungarish and T. Zemach, On axisymmetric intrusive gravity currents in a stratified ambient—shallow-water theory and numerical results, *Eur. J. Mech. B-Fluid* **26** (2007) 220–235.
14. T. von Kármán, The engineer grapples with nonlinear problems, *Bull. Amer. Math. Soc.* **46** (1940) 615–683.
15. T. B. Benjamin, Gravity currents and related phenomena, *J. Fluid Mech.* **31** (1968) 209–248.
16. M. A. Hallworth, J. C. Phillips, H. E. Huppert and R. S. Sparks, Entrainment in turbulent gravity currents, *Nature* **362** (1993) 829–831.

Appendix A. The value of A_0

The constant A_0 as stated, but not derived, in (6), is given by

$$A_0 = \left(\frac{27\,\mathrm{Fr}^2}{12 - 2\,\mathrm{Fr}^2} \right)^{1/3}, \tag{A.1}$$

in the 2D case we are considering, where Fr is the Froude number, a parameter satisfying, when the Boussinesq approximation is made, [via von Kármán (14)]

$$\mathrm{Fr}^2\, g' h\,(x_N,\ t) = \dot{x}_N^2. \tag{A.2}$$

Grundy and Rottman, in (6), state that $\mathrm{Fr} \approx 1$ [meaning that $A_0 = (27/10)^{1/3}$, which is approximately 1.39] for small enough values of $\left(\rho_{\mathrm{heavier}} - \rho_{\mathrm{lighter}}\right)/\rho_{\mathrm{heavier}}$, but there is no general agreement on this value. References (14) and (15) derive a theoretical value of $\sqrt{2}$, albeit using different methods of solving the same inviscid Euler equation, and (5) suggests a value of 1.19, from experimental observations, which include, naturally, turbulent entrainment into the gravity current (16). We follow the convention of (6) in this article, taking $\mathrm{Fr} = 1$, unless otherwise stated.

In the axisymmetric case, we instead take

$$A_0 = \left(\frac{16\,\mathrm{Fr}^2}{\pi\,(4 - \mathrm{Fr}^2)} \right)^{1/4}. \tag{A.3}$$